Applied Catalysis B: Environmental 301 (2022) 120755

Contents lists available at ScienceDirect

Applied Catalysis B: Environmental

journal homepage: www.elsevier.com/locate/apcatb

Carbon dots mediated charge sinking effect for boosting hydrogen evolution in Cu-In-Zn-S QDs/MoS_2 photocatalysts

Qitao Chen [a,1], Yanhong Liu [a,1], Xiaoqing Gu [b,1], Di Li [a], Dongxu Zhang [a], Dongqi Zhang [a], Hui Huang [b], Baodong Mao [a,*], Zhenhui Kang [b,c,**], Weidong Shi [a,*]

[a] School of Chemistry and Chemical Engineering, Jiangsu University, 301 Xuefu Road, Zhenjiang 212013, China
[b] Institute of Functional Nano and Soft Materials (FUNSOM), Jiangsu Key Laboratory for Carbon-based Functional Materials and Devices, Soochow University, Suzhou 215123, China
[c] Macao Institute of Materials Science and Engineering, Macau University of Science and Technology, Taipa 999078, Macau SAR, China

ARTICLE INFO

Keywords:
Photocatalysis
Carbon dots
CIZS QDs
Charge extraction
Transient photovoltage spectroscopy

ABSTRACT

Visible-driven photocatalysis plays a critical role in solar energy conversion, but the efficiency is limited by the poor charge separation and utilization. Here, a ternary photocatalyst is constructed using Cu-In-Zn-S quantum dots (CIZS QDs), MoS_2 and carbon dots (CDs). Interestingly, transient photovoltage measurements confirm that MoS_2 has no assistance on the charge extraction rate, whereas CDs dramatically increases the attenuation constant of the charge recombination process (from 0.178 to 0.260 ms) due to its electron sinking effect. The optimal hydrogen production rate of CIZS/MoS_2/CDs reaches 3706 μmol g^{-1} h^{-1}, which is 6.65 and 148.24 times to that of CIZS QDs and MoS_2, respectively. Further electrocatalytic tests indicate that MoS_2 is the main place for hydrogen evolution reaction, whereas CIZS and CDs are responsible for light harvesting and charge sinking, respectively. This work provides a useful guideline for the synergy of charge extraction and utilization process in composite photocatalyst design.

1. Introduction

Photocatalytic water splitting has been regarded as a promising way to obtain hydrogen, an important alternative form of storable and clean energy in the future [1–3]. Considering the distribution of solar spectrum, large effort has been contributed to the development of visible-active photocatalysts [4–6]. Among them, narrow-bandgap quantum dots (QDs) have attracted much attention due to their widely adjustable band gap, large specific surface area, short charge transfer distance and tunable photoelectric properties, which enable efficient light harvesting and charge separation [7–11]. However, the photocatalytic activity and stability of QD photocatalysts are still far below expectation, suffering from the abundant defect states and severe electron-hole recombination [12]. More and more studies show that poor charge separation is the main cause of photo corrosion and stability issues. For this purpose, a series of strategies have been proposed, including doping [13], nanostructure control [14], heterojunction construction [15], and cocatalyst loading [16].

Among these methods, the cocatalysts played a crucial role in promoting the separation and utilization of photogenerated charge carriers [17]. The 2D transition-metal dichalcogenides, like molybdenum disulfide (MoS_2), had gained significant interest due to the unique structure with unsaturated Mo and S active sites on the edge and remarkable catalytic properties [18–20]. Recent studies showed that MoS_2 could be used as an effective hydrogen evolution cocatalyst [21,22] when combined with II-VI and I-III-VI QDs, where the shared sulfur lattice was beneficial to reduce the interface defects and charge recombination [23,24]. These 0D/2D QD/nanosheet composites provide an ideal structure model for photocatalysts by embedding high-activity QDs onto 2D nanosheets with fast charge transfer. However, since the active sites of MoS_2 are mainly distributed on the edge, the photocatalytic efficiency is still limited due to the slow charge transfer within the 2D Mo-S planes [25]. Large efforts have been contributed to the design of MoS_2 nanostructures, such as ultrathin nanosheets, doping and exfoliation into

* Corresponding authors.
** Corresponding author at: Institute of Functional Nano and Soft Materials (FUNSOM), Jiangsu Key Laboratory for Carbon-based Functional Materials and Devices, Soochow University, Suzhou 215123, China.
E-mail addresses: maobd@ujs.edu.cn (B. Mao), zhkang@suda.edu.cn (Z. Kang), swd1978@ujs.edu.cn (W. Shi).
[1] These authors contributed equally to this work.

https://doi.org/10.1016/j.apcatb.2021.120755
Received 28 June 2021; Received in revised form 28 August 2021; Accepted 24 September 2021
Available online 29 September 2021
0926-3373/© 2021 Elsevier B.V. All rights reserved.

monolayers to improve the performance hydrogen evolution [26–28]. However, special charge transfer design and kinetics study are still required towards the increased charge extraction, storage and utilization.

In photocatalysis, carbon dots (CDs) have attracted much attention on increasing light absorption, promoting charge separation and acting as surface active sites due to their unique physical and chemical properties [29,30]. More importantly, the introduction of CDs can not only accelerate the separation of photogenerated carriers, but also serve as electron donors and acceptors, which is crucial for long-lived charge carriers [31–33]. These unique properties make CDs an important multifunctional component in photocatalytic systems. For instance, the compositing of CdS QDs and CDs proved that CDs had excellent electron storage capability that is important for promoting the photocatalytic activity [34]. Moreover, CDs acted as electron acceptors in the NiS/CDs/CdS system with efficient charge transfer and hydrogen production [31]. The introduction of CDs could also significantly increase the electrocatalytic hydrogen evolution reaction (HER) activity in MoS_2 due to its photo-induced electron transfer property [30]. However, most existing studies only considered the efficient separation of electrons and holes, without any further consideration for the whole photocatalytic system and the related mechanism.

Cd-free I-III-VI QDs represented a class of the most promising photocatalysts owning to their widely tunable bandgap and long lifetime [35]. Herein, in order to achieve synergetic charge extraction and conversion, CDs with the electron storage function were introduced with MoS_2 together to modify CIZS QDs, forming CIZS/MoS_2/CDs ternary composites. Transient photovoltage (TPV) spectroscopy was used to demonstrate the promoted charge extraction and inhibited charge recombination by CDs in the composites, where MoS_2 did not contribute much on the charge extraction rate but on the surface HER. The kinetic studies showed the dominant role of CDs by high charge extraction efficiency, short extraction time, and long attenuation constant. As a result, the hydrogen production rate of the composite achieved 3706 $\mu molg^{-1}h^{-1}$, which was 6.65 times to that of pure CIZS QDs and 148.24 times to that of MoS_2. It was further confirmed, for the first time, the critical role of effective surface charges on photocatalytic efficiency brought by the binary 0D/2D CDs/MoS_2 cocatalyst, in which CDs acted as a platform for electron sinking and MoS_2 provided the main active sites of HER, rather than the commonly mentioned charge extraction effect. This work pointed out an important direction for the design of efficient and stable composite photocatalysts via the comprehensive consideration of charge extraction, sinking and conversion.

2. Experimental section

2.1. Chemicals

All reagents were obtained from Sinopharm Chemical Reagent Co. Ltd without any further purification, including copper nitrate ($Cu(NO_3)_2.H_2O$), zinc acetate ($Zn(OAc)_2•2H_2O$), indium nitrate ($In(NO_3)_3•4.5H_2O$), thioacetamide, sodium hydroxide (NaOH), L-cysteine, L-ascorbic acid, hexaammonium heptamolybdate tetrahydrate ($(NH_4)_6Mo_7O_{24}.4H_2O$), thiourea (CH_4N_2S), hydrochloric acid (HCl), ethanol, citric acid, ethylenediamine, polyvinyl pyrrolidone ($(C_6H_9NO)_n$, PVP) and oleic acid ($C_{18}H_{34}O_2$). Dialysis membrane (MWCO: 200 Da) was purchased from Shenzhen Bymerson Scientific Instrument Co., Ltd.

2.2. Synthesis of CIZS/MoS_2/CDs

The CIZS QDs, MoS_2 nanosheets, and CDs were synthetized referring to previous work with modifications [12,35–40]. The details are shown in the Supporting Information.

CIZS/MoS_2 nanocomposites were obtained by simple mechanical stirring [40]. Briefly, different amount of 12 mg/mL CIZS QDs solution (1.65, 1.62, 1.50 and 1.56 mL) was added to water (13.15, 12.80, 12.46 and 12.13 mL) followed by ultrasonication at room temperature for 30 min to achieve a homogeneous dispersion. At the same time, 1 mg/mL MoS_2 solution was also treated by ultrasound. Then, certain amounts of MoS_2 solution (0.198, 0.582, 0.952 and 1.310 mL) were added to CIZS QDs solution and magnetically stirred for 12 h. According to the amount of MoS_2, the acquired samples were denoted as CIZS/MoS_2-1%, CIZS/-MoS_2-3%, CIZS/MoS_2-5% and CIZS/MoS_2-7%.

Preparation of CIZS/MoS_2/CDs nanocomposites was carried out by hydrothermal treatment. Specifically, 15 mL of 1 mg/mL CIZS/MoS_2 nanocomposites was mixed with certain amount of 20 mg/mL CDs solution (9.0, 26.5, 43.0, 59.5 and 75.0 μL) and stirred for 1 h. Subsequently, the above mixed solution was put in a Teflon-lined steel autoclave and kept at 110 °C for 4 h. After cooling down, it was washed with ethanol/water for three times. According to the amount of CDs, the acquired samples were denoted as CIZS/MoS_2/CDs-1%, CIZS/MoS_2/CDs-3%, CIZS/MoS_2/CDs-5% and CIZS/MoS_2/CDs-7% and CIZS/MoS_2/CDs-9%. Finally, the samples were kept in deionized water and stored for further use.

2.3. Characterizations

X-ray diffraction (XRD) was used to analyze the samples ranged from 10° to 80° (scan rate: 7.0°/min) with Cu Kα radiation source (λ = 1.5417 Å) on a D/MAX-2500 diffractometer (Empyrean, Holland Panalytical). Raman spectroscopy with a scan range of 100−3000 cm^{-1} was measured using an America DXR. The transmission electron microscope (TEM), high-resolution TEM (HRTEM) and elemental mapping were measured on a Tecnai G2 F30 STWIN electron microscope. Energy dispersive X-ray spectroscopy (EDX 1800 ROHS) was carried out to analyze the content of the elements. X-ray photoelectron spectroscopy (XPS) measurements were conducted on a KRATOS Axis ultra-DLD spectrometer with a monochromatic Al Kα X-ray source (hυ = 1283.3 eV). UV–vis diffuse reflectance spectra were characterized through a Cary 8454 spectrometer. A Cary Eclipse fluorescence spectrophotometer was used for photoluminescence (PL) of QDs. Time-resolved PL spectra were collected by excitation at 481 nm using a QuantaMaster TM 40 spectrometer (Photon Technology International, Inc.) [41,42]. Transient photovoltage (TPV) was measured on a home-made system, which was excited by a nanosecond laser radiation pulse (wavelength of 355 nm and repetition rate of 5 Hz) from a third harmonic Nd:YAG laser (Beamtech Optronics Co., Ltd). Electrochemical impedance spectra (EIS) and photocurrent response of samples uniformly distributed on fluoroalkane doped tin oxide (FTO) glass were measured on a CHI 760E electrochemical workstation (Chenhua, China) with a standard three-electrode cell and 0.5 M Na_2SO_4 solution as the electrolyte. In a typical process, 0.01 g of the as-obtained catalyst was dispersed in a solution containing 1 mL of ethanol, 5 mg of PVP and 0.02 ml of oleic acid. Afterwards, the solution was ultrasonically stirred for 30 min. Then, the solution was gradually applied to a clean 1 × 2 cm^2 FTO glass electrode using a spin coater. The photocurrent was measured under illumination of a 300 W xenon lamp. The HER properties of all samples were performed in a typical three-electrode system using CHI 760E (Chenhua, Shanghai China) with the CIZS QDs, MoS_2 nanosheets and CIZS/MoS_2/CDs on FTO as the working electrodes, a graphite rod as the counter electrode and Ag/AgCl electrode as the reference electrode.

2.4. Photocatalytic H_2 evolution

The samples were estimated for photocatalytic performance under visible light through a Multi-channel photochemical reaction system (PCX-50B Discover, Beijing Perfectlight, China). Commonly, 20 mg of the previously synthesized photocatalysts were dispersed in 15 mL aqueous solution of 0.2 M L-ascorbic acid as the sacrificial agent, which was subsequently transferred to a 40 ml reaction vial. Next, the mixed solution was bubbled with nitrogen for 15 min. Then the whole reaction system was irradiated

with the white LED light (100 mW/cm^{-2}) for 5 h. Under vigorous stirring, the generated gas products (1.5 mL) were extracted every one hour and injected into a gas chromatography (GC-7900) with a TCD detector. The apparent quantum efficiency (AQE) over CIZS/MoS_2/CDs was measured with a series of monochromatic LEDs to provide light at different wavelengths (λ = 420, 450, 485, 520, 595 and 630 nm) for photocatalytic hydrogen evolution under similar reaction conditions. Then, according to the number of evolved H_2 molecules and incident photons, AQE at different wavelengths was calculated. The specific calculation process and results are displayed in Table S4 in Supporting Information.

3. Results and discussion

3.1. Structural characterization of the photocatalysts

The structure, size and morphology of the photocatalysts were characterized by TEM. TEM images of CIZS QDs and CDs are shown in Fig. 1a and b, respectively. CIZS QDs (Fig. 1a) show a quasi-spherical shape with a size distribution of about 4.5 ± 0.5 nm. CDs (Fig. 1b) are also spherical in shape with a size distribution of about 2.5 ± 0.5 nm. Fig. 1c and Fig. S1a show the TEM and HRTEM images of MoS_2 nanosheets, which revealed the exposed ultrathin layer structure. Fig. S1b is the TEM image of CIZS/MoS_2, which proves that the CIZS QDs were attached to the surface of MoS_2. Fig. 1d exhibits the TEM image of CIZS/MoS_2/CDs composite, showing that CIZS QDs and CDs were successfully constructed on the MoS_2 nanosheets with a close 0D/2D heterojunction structure. HRTEM image (Fig. 1e) of CIZS/MoS_2/CDs composite further shows the 0.31 nm lattice spacing that is in excellent agreement with the (112) plane of CIZS [37]. The 0.32 nm lattice spacing corresponds the (110) plane of MoS_2 [43], and the lattice spacing of 0.21 nm is attributed to (101) plane of graphite of CDs [38]. The scanning TEM (STEM, Fig. 1f), EDX overlap and element mapping images (Fig. 1g) of CIZS/MoS_2/CDs displayed that all the Cu, In, Zn, S, Mo, C, N and O elements could be observed with uniform distribution, indicating that CDs and CIZS QDs were successfully loaded and well dispersed on MoS_2 in the nano-composites.

To explore the structure of the CIZS QDs, MoS_2 and CDs, the photocatalysts were first characterized by XRD. The XRD pattern of CDs (Fig. 2a) showed a wide diffraction peak at 26°, corresponding to the (002) plane of hexagonal graphitic carbon [44]. Diffraction peaks in CIZS at 27.3°, 47.1° and 55.3° well matched with (112), (204) and (312) crystal planes of chalcopyrite phase $Cu_{0.412}In_{0.412}Zn_{0.175}S$ (JCPDS No. 47–1371), respectively. Diffraction peaks at 14.8°, 32.7°, 39.2°, 48.4° and 58.1° well matched with the (002), (100), (103), (105) and (110) crystal planes of hexagonal phase MoS_2 (JCPDS No. 37–1492). CIZS/MoS_2/CDs showed similar diffraction peaks with that of CIZS, indicating the addition of MoS_2 and CDs did not change the crystal structure of CIZS QDs. The XRD diffraction peaks of MoS_2 and CDs are very low in the composite possibly because of their low loading amount and the shielding by QDs deposited on the surface of the nanosheets. This

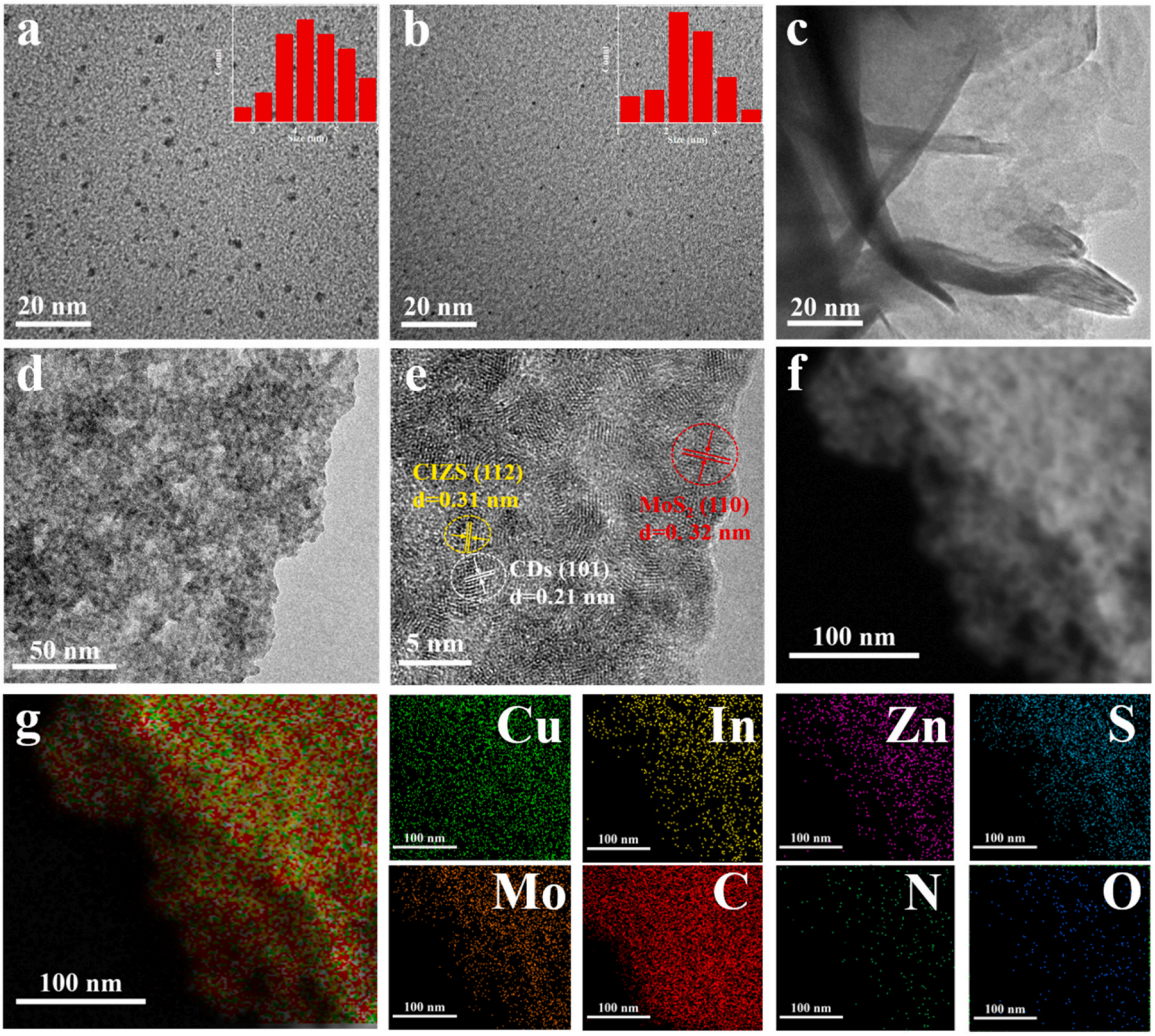

Fig. 1. TEM images of (a) CIZS QDs, (b) CDs, (c) MoS_2 nanosheets and (d) CIZS/MoS_2/CDs. Insets in (a) and (b): size distribution of the CIZS QDs and CDs, respectively. (e) HRTEM, (f) HAADF-STEM, and (g) corresponding elemental mapping images of CIZS/MoS_2/CDs.

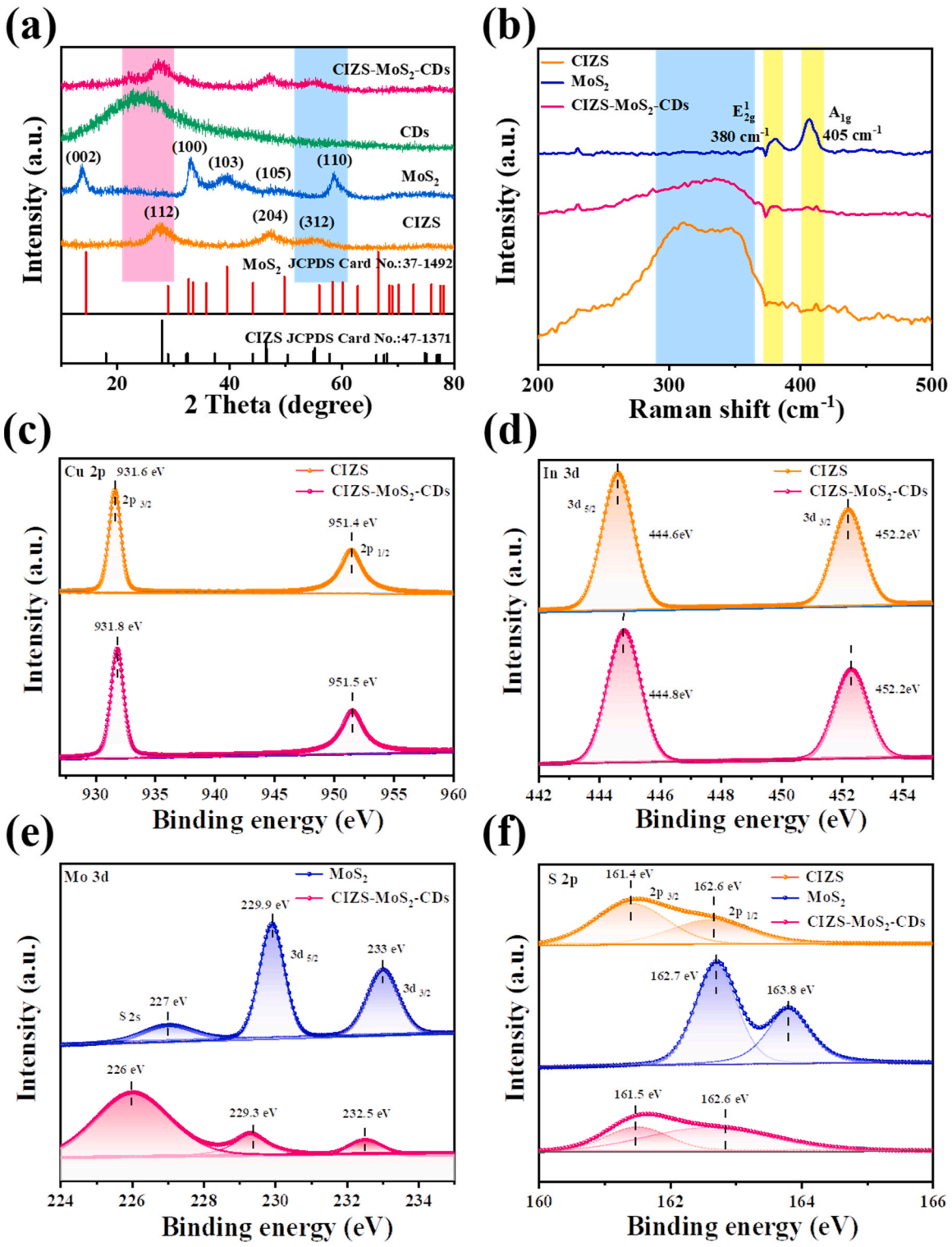

Fig. 2. (a) XRD patterns and (b) Raman spectra of the samples. High-resolution XPS spectra of (c) Cu 2p and (d) In 3d for CIZS and CIZS/MoS_2/CDs, (e) Mo 3d for MoS_2 and CIZS/MoS_2/CDs, and (f) S 2p for CIZS, MoS_2 and CIZS/MoS_2/CDs.

phenomenon was also observed in other reports of MoS_2 or CDs composites [38,45]. To further study the effect of CDs in the nanocomposites, we prepared a series of CIZS/MoS_2/CDs with different contents of CDs. With the increase of CDs content, the diffraction peak of CIZS/MoS_2/CDs near 27° became wider (Fig. S2), which can be ascribed to the fact that CDs have a wide diffraction peak near 26° close to the (112) peak of CIZS QDs at 27.3°, resulting in its widening. To further prove the existence and actual ratio of MoS_2 and CDs, EDX was detected on the composites (Fig. S3), which clearly indicates the presence of all seven elements with Mo ratios of 5.93%, 5.47%, 5.86% and 5.18%, and C ratios of 1.90%, 3.24%, 5.40% and 7.88% in CIZS+MoS_2-5%+CDs-1%, CIZS+MoS_2-5%+CDs-3%, CIZS+MoS_2-5%+CDs-5% and CIZS+MoS_2-5%+CDs-7%, respectively. The above results show that the 0D/2D composite photocatalysts were successfully synthesized and the interface contact was very close. Raman spectra (Fig. 2b) were further acquired to study the structure of CIZS/MoS_2/CDs. The wide peak in

CIZS/MoS_2/CDs at 315 cm^{-1} was the PL signal of CIZS [40]. The Raman spectrum of CDs (Fig S4) has two peaks near 1303 and 1386 cm^{-1}, which came from D band of sp^3 carbon in disordered carbon and G band of sp^2 carbon in-plane vibration. Appearance of the two peaks at 380 cm^{-1} and 405 cm^{-1} of MoS_2 revealed the existence of MoS_2 with the characteristic E^1_{2g} and A_{1g} vibrational modes [39]. Compared with pure CIZS QDs and MoS_2, CIZS/MoS_2/CDs showed a wide peak around 300–360 cm^{-1} similar to that of CIZS, and two broader and lower peaks at 380 and 405 cm^{-1} similar to that of MoS_2 nanosheets, indicating that they were successfully combined with CIZS QDs [12,40,43].

XPS was used to prove the existence and the corresponding valence states of all elements in CIZS/MoS_2/CDs. XPS survey spectra (Fig. S5) confirmed that the corresponding elements existed in CIZS, MoS_2 and CIZS/MoS_2/CDs. High resolution XPS spectra of Cu are displayed in Fig. 2c, in which the binding energies of Cu 2p were located at 931.8 and 951.5 eV, owing to Cu $2p_{3/2}$ and $2p_{1/2}$ of Cu^+ [37], respectively. In Fig. 2d, two distinct peaks of In located at 444.8 and 452.2 eV, which can be attributed to In $3d_{5/2}$ and $3d_{3/2}$ in In^{3+} [46], respectively. In addition, there were two distinct peaks at 1021.6 and 1044.7 eV in Fig. S6, attributing to Zn $2p_{3/2}$ and Zn $2p_{1/2}$, respectively. Fig. 2e showed the binding energies of Mo 3d located at 229.3 and 232.5 eV, owing to Mo $3d_{5/2}$ and $3d_{3/2}$ of Mo^{4+} [39], respectively. According to Fig. 2f, the binding energies of S 2p were located at 161.5 and 162.6 eV, proving the presence of S^{2-} [47]. Compared with pure CIZS QDs, binding energies of all elements in CIZS/MoS_2/CDs shifted slightly to a higher binding energy, indicating partial electron transfer to the surface of MoS_2, which revealed the close contact in favor of photogenerated charge carrier transfer [40]. Compared with the pristine MoS_2, the binding energies of Mo and S elements in the CIZS/MoS_2/CDs have a slight blue shift, which reveals a close interface contact favorable for charge transfer and proves the role of MoS_2 as electron acceptor [5].

3.2. Optical properties and band alignment of the photocatalysts

The light-harvesting ability of the photocatalysts was studied by UV–vis diffuse reflectance spectroscopy, and the band gaps were estimated accordingly. UV–vis reflectance spectra (Fig. 3a) demonstrate an absorption edge of QDs around 660 nm and absorption of MoS_2 in the full visible range, similar to previous report [41]. In addition, the brownish CDs sample absorbs light from UV to near IR. After introducing MoS_2 and CDs, the light absorption capability of CIZS/MoS_2/CDs increased gradually in the long-wavelength range, e.g., the addition of MoS_2 and CDs improved the light harvesting ability of CIZS in the visible range. According to the UV–vis absorption data and the formula:

$$ah\nu = A(h\upsilon - E_g)^{1/2} \quad (1)$$

we can obtain the Tauc plots [48] (Fig. 3b) and calculate the band gaps of CIZS and MoS_2, which were 2.02 and 1.20 eV, respectively. Next, the XPS valence band (VB) spectra (Fig. 3c) indicated VB positions of 0.87 and 1.14 eV for CIZS and MoS_2, respectively. The conduction band (CB) position was obtained according to the formula:

$$E_{VB} = E_g + E_{CB} \quad (2)$$

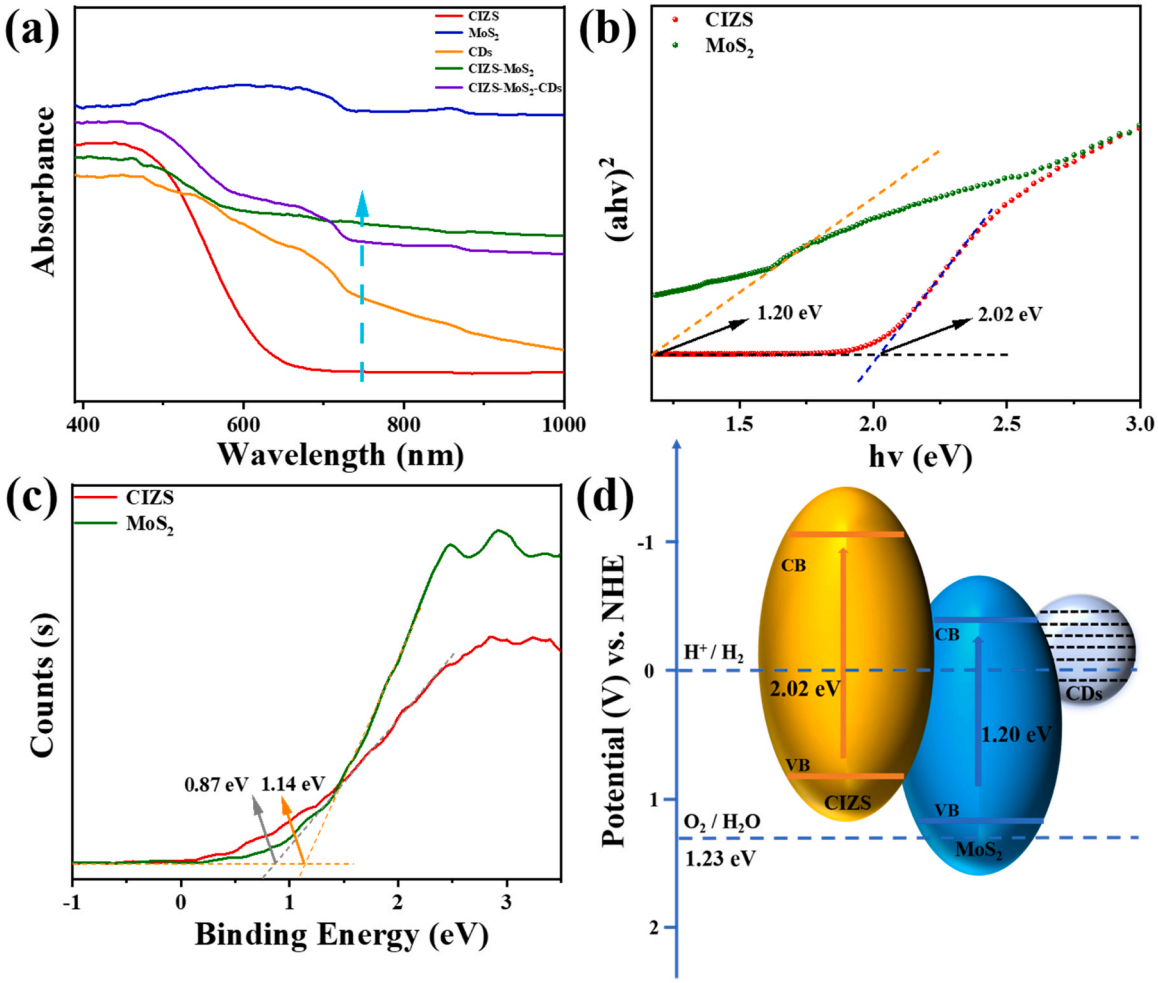

Fig. 3. (a) UV–vis diffuse reflectance spectra of CIZS QDs, MoS_2, CDs, CIZS/MoS_2, and CIZS/MoS_2/CDs. (b) Tauc plots of CIZS QDs and MoS_2. (c) XPS valence band spectra of CIZS QDs and MoS_2. (d) Corresponding band alignment diagram.

Then the band alignment diagram (Fig. 3d) was gained. It shows that the band structure of the CIZS/MoS_2/CDs composite was beneficial to the charge transfer from CIZS to MoS_2 and the subsequent photocatalytic hydrogen production.

3.3. Study of the interfacial kinetics

TPV of CIZS, MoS_2 and CDs. Charge transfer and recombination rates on the catalyst surface are the key parameters to understand the catalytic mechanism [49]. TPV of CIZS, MoS_2 and CDs were performed to further study the kinetics of interfacial charge extraction and recombination processes. Fig. 4a showed a photovoltage intensity trend of MoS_2 > CDs > CIZS, where MoS_2 also acts as a strong light absorption unit in addition to CIZS, different from previous reports [16]. The enlarged diagram of t_{max} values (the time required for the intensity to reach the maximum) of three samples are shown in Fig. 4b., in which t_{max} of CDs (t_{max3}=0.085 ms) was much shorter than that of CIZS (t_{max1}, 0.128 ms) and MoS_2 (t_{max2}, 0.110 ms), illustrating the fastest charge extraction rate (or electron diffusion rate) of CDs. The integral area (A) in TPV represents the cap ability of the catalysts to produce photoinduced electrons. Fig. 4c displays that the charge extraction efficiency of MoS_2 (A_2, 0.050) is actually greater than that of CIZS (A_1, 0.010) and CDs (A_3, 0.023), suggesting MoS_2 has the highest amount of charge extraction. Furthermore, the charge recombination process of CIZS, MoS_2 and CDs (Fig. 4d) can be roughly estimated by the attenuation constants (τ) from fitting of the normalized TPV decay curves. The τ of CIZS (τ_1, 0.178 ms) and MoS_2 (τ_2, 0.196 ms) are much longer than that of CDs (τ_3, 0.117 ms), indicating a relatively slower charge recombination rate of CIZS and MoS_2.

TPV of CIZS/MoS_2 vs. CIZS QDs. In order to further study the role of MoS_2 in the composite system, the TPV relaxation curve of CIZS/MoS_2 was compared with pure CIZS QDs. According to Fig. 5a, TPV curves indicate that CIZS/MoS_2 has much higher photovoltage intensity than CIZS. Fig. 5b shows that CIZS/MoS_2 (t_{max4}, 0.101 ms) has almost the same charge extraction rate to that of pure QDs (t_{max1}, 0.104 ms), different from the commonly reported effect of promoted charge extraction by MoS_2. The shaded area A of the integral fitting in Fig. 5c represents the charge extraction efficiency. A_4 of CIZS/MoS_2 is 0.039, which is 3.90 times to that of CIZS (A_1, 0.010), indicating that more photogenerated electrons were generated and successfully extracted onto the surface of CIZS/MoS_2 with the introduction of MoS_2. This is consistent with the absorption spectra (Fig. 3a) and high photovoltage intensity of MoS_2 (Fig. 4a). According to Fig. 5d, the attenuation constants (τ) of charge recombination process of CIZS/MoS_2 and CIZS are 0.192 (τ_4) and 0.178 ms (τ_1), respectively, indicating a slightly slower charge recombination rate of CIZS/MoS_2, which is conducive to the hydrogen production reaction [11]. As a result, the introduction of MoS_2 on CIZS QDs had no assistance on the electron extraction rate (in contrast to commonly reported results [24]), but contributed dramatically on the light harvesting and the amount of extracted charge carriers.

TPV of CIZS/MoS_2/CDs vs. *CIZS QDs.* To further study the critical role of CDs in the composite system, the TPV relaxation curve of CIZS/MoS_2/CDs was further compared with pure CIZS QDs. In Fig. 6a, TPV relaxation curves indicate that CIZS/MoS_2/CDs has much higher

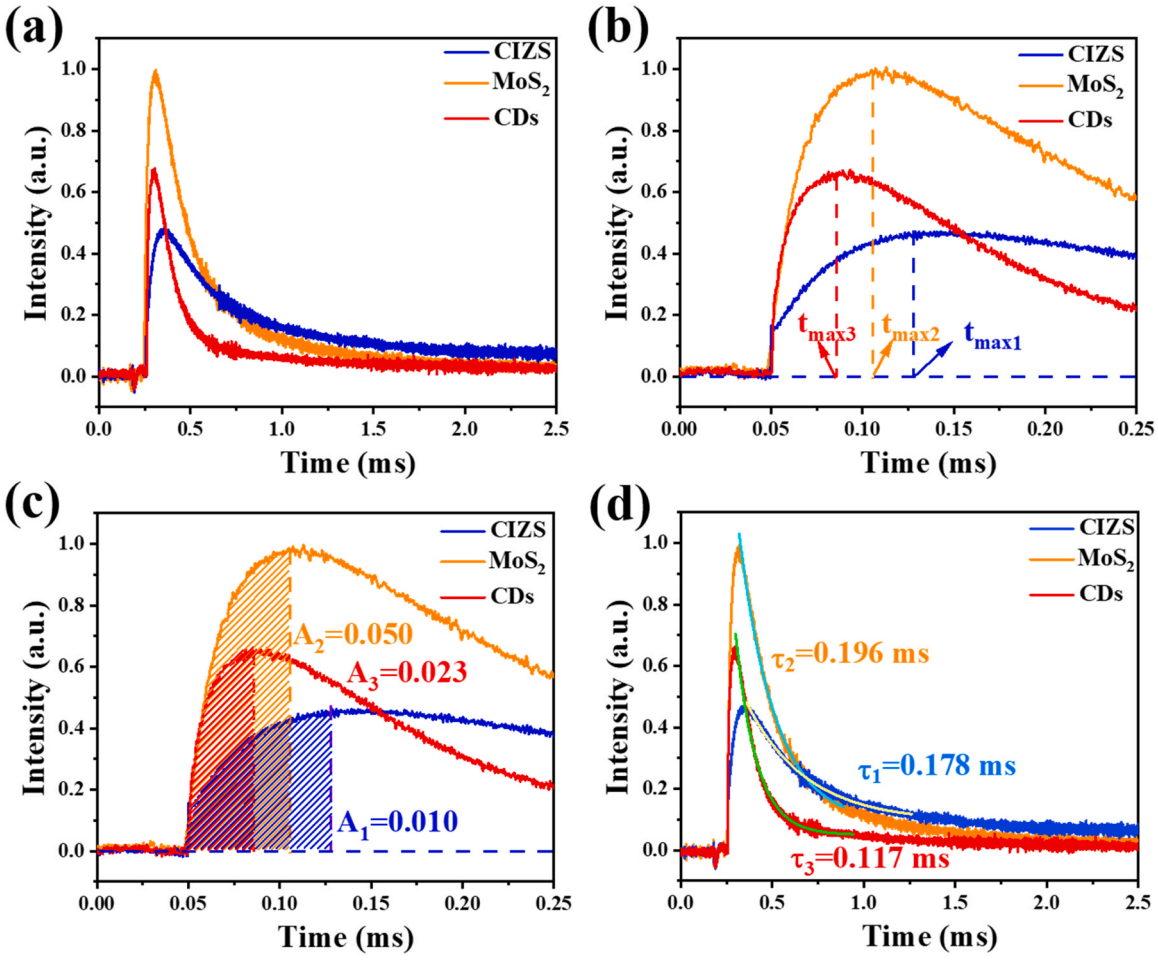

Fig. 4. (a) TPV relaxation curves, (b) corresponding maximum charge extraction time (t_{max}), (c) amount of charge extraction (A), and (d) attenuation constants (τ) of charge recombination process of CIZS QDs, MoS_2 nanosheets and CDs.

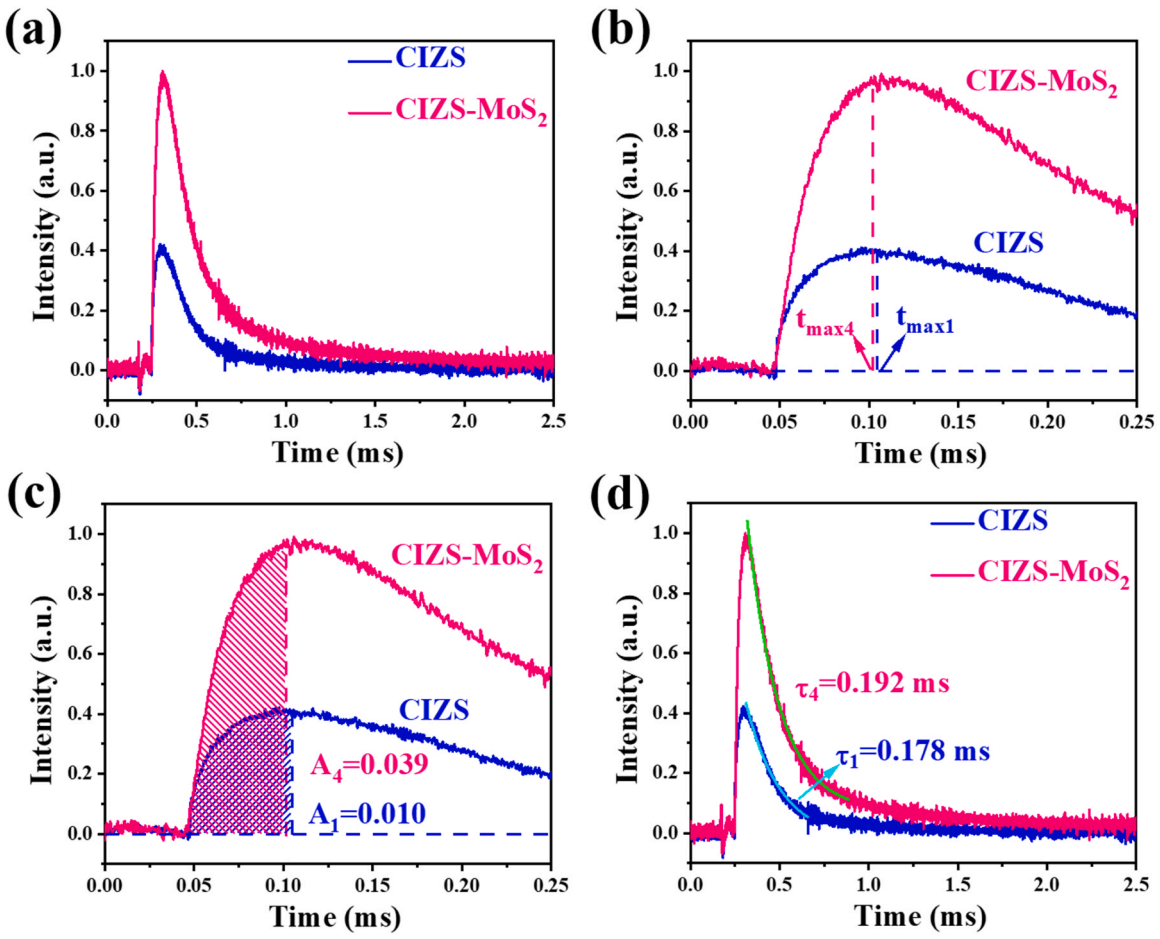

Fig. 5. (a) TPV relaxation curves, (b) corresponding maximum charge extraction time (t_{max}), (c) amount of charge extraction (A), and (d) attenuation constants (τ) of charge recombination process of CIZS QDs and CIZS/MoS_2.

photovoltage intensity than that of CIZS. However, Fig. 6b shows that CIZS/MoS_2/CDs (t_{max5}, 0.104 ms) has almost the same electron extraction time with pure QDs (t_{max1}, 0.109 ms). In Fig. 6c, the maximum charge extraction efficiency A_5 of CIZS/MoS_2/CDs is 0.056, 5.60 times larger than that of CIZS (A_1, 0.010), indicating that more photogenerated electrons were transferred to the surface of CIZS/MoS_2/CDs. According to Fig. 6d, the attenuation constant τ of CIZS/MoS_2/CDs were 0.260 (τ_5) ms. Although CDs have a relatively short τ_3 of 0.117 ms, τ_5 of CIZS/MoS_2/CDs is dramatically larger than that of CIZS (τ_1, 0.178 ms), or CIZS/MoS_2 (τ_4, 0.192 ms), which is a strong evidence that the charge recombination of CIZS/MoS_2/CDs was restricted with the introduction of CDs. This can be attributed to the charge storage characteristics (or electron sinking effect) of CDs that benefits the charge separation efficiency and lifetime elongation in CIZS/MoS_2/CDs [49].

From the above analysis of the TPV data of CIZS QDs, CIZS/MoS_2 and CIZS/MoS_2/CDs, we can draw a conclusion that the strong photoelectronic effect of CIZS/MoS_2/CDs is mainly due to the light response of MoS_2 and the charge sinking effect of CDs. With the addition of CDs, the recombination of photogenerated electrons and holes was slowed down in CIZS/MoS_2/CDs. In fact, CDs promoted the charge carrier lifetime, which was different from the previously reported effect of charge extraction rate or efficiency [29]. In the ternary system, t_{max} value remains unchanged, whereas A and τ values were increased by 5.60 and 1.46 times to that of CIZS, respectively, due to the charge sinking characteristics of CDs that can benefit the surface charge accumulation and subsequent hydrogen evolution reaction.

3.4. Photocatalytic activity and interface kinetics

To explore the photocatalytic performance, with L-ascorbic acid as the sacrificial agent, the samples were irradiated for 5 h with wavelengths ≥420 nm. The hydrogen production of all samples increased linearly with irradiation time (Fig. 7a). It worths nothing that there is little activity under dark conditions (with CIZS/MoS_2/CDs) and photolysis of AA without catalyst. In addition, MoS_2 itself produces very little hydrogen (Fig. 7b), which may be due to its low CB position and poor charge separation. CIZS/MoS_2/CDs (3.706 mmol g^{-1} h^{-1}) showed the best hydrogen production rate, which was 6.65 times and 148.24 times of that pure CIZS (0.557 mmol g^{-1} h^{-1}) and MoS_2 (0.025 mmol g^{-1} h^{-1}), respectively. Compared with binary CIZS/MoS_2, CIZS/MoS_2/CDs was also increased by 2.32 times. It can be attributed to the introduction of MoS_2 and CDs that increases the active sites and accelerates the charge transfer.

To better understand the large improvement of catalytic performance, a systematic comparison of TPV data is shown in Fig. 7(c-f). With the addition of the multicomponents, t_{max} of CIZS (0.105 ms), CIZS/MoS_2 (0.102 ms) and CIZS/MoS_2/CDs (0.102 ms) were basically unchanged, which indicates that the introduction of CDs and MoS_2 in the ternary nanocomposites has little effect on the charge extraction rate, in contrast to the commonly reported results [30]. Fig. 7d showed the maximum amount of extracted electrons (A) of the samples, indicating a 5.6 times improvement of CIZS/MoS_2/CDs (A_5, 0.056) than pure CIZS (A_1, 0.010) that is much larger than that of modification MoS_2 (A_4, 0.039). This result showed that the electron sinking effect of CDs greatly improved the charge extraction efficiency. Fig. 7e showed the τ values of

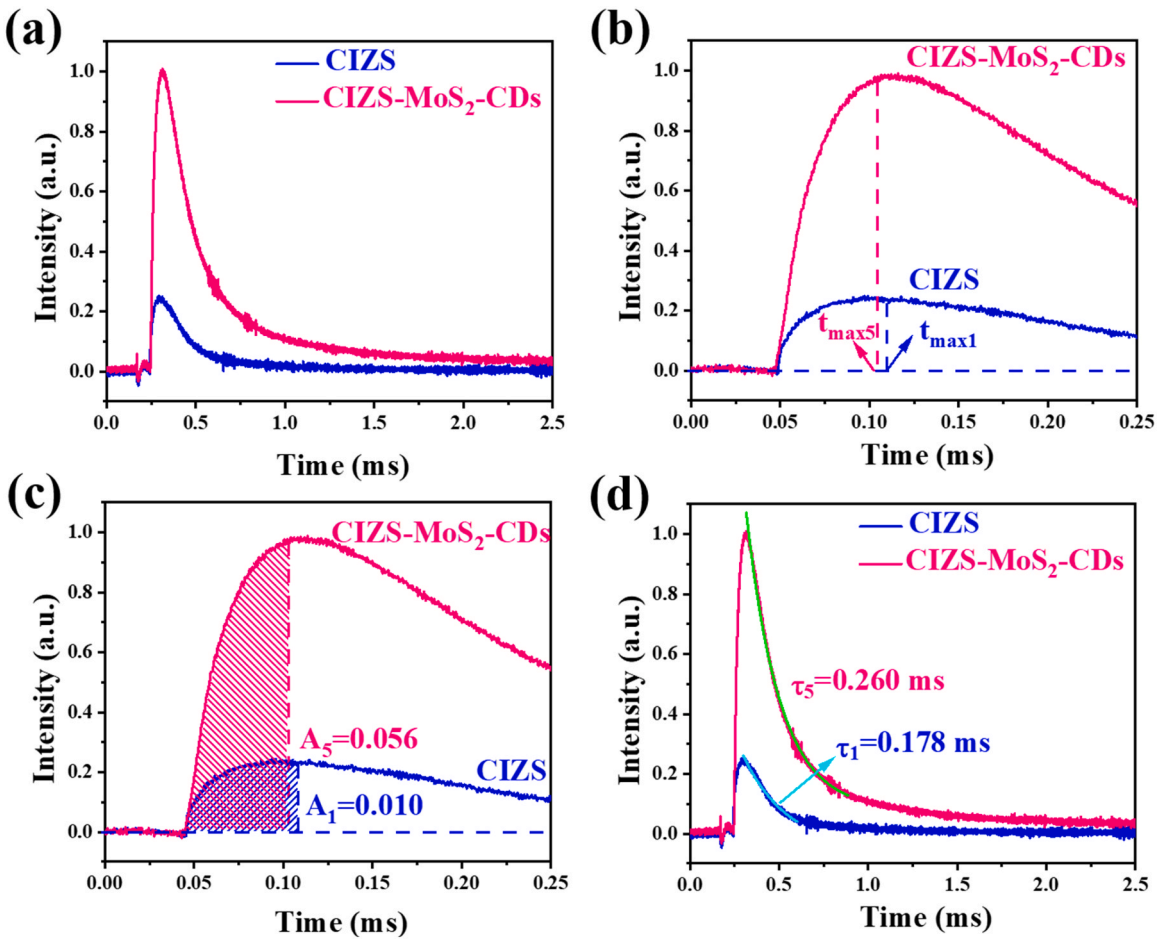

Fig. 6. (a) TPV relaxation curves, (b) corresponding maximum charge extraction time (t_{max}), (c) amount of charge extraction (A), and (d) attenuation constants (τ) of charge recombination process of CIZS QDs and CIZS/MoS_2/CDs.

different samples. The larger the τ, the slower the charge recombination. The charge recombination of CIZS/MoS_2/CDs (τ_5, 0.260 ms) was largely restricted compared to CIZS/MoS_2 (τ_4, 0.192 ms) and pure CIZS (τ_1, 0178 ms), attributing to the effective improvement of charge storage after the introduction of CDs. The results show that CDs and MoS_2 have the synergistic effect of electron extraction.

Moreover, the amount of the effective surface electrons can be obtained by $A_{eff}=\frac{A\times\tau}{t_{max}}$, which is a useful parameter for evaluating the final efficiency of charge carrier conversion. Fig. 7f shows the dramatic increase of the effective surface charge from CIZS (0.016), CIZS/MoS_2 (0.074) to CIZS/MoS_2/CDs (0.140). The main reason can be ascribed to the electron sinking effect of CDs that led to a restriction in charge recombination, so that more electrons could be extracted, along with longer lifetime. To sum up, it was beyond expectation that MoS_2 itself was a light absorption unit with high photovoltage intensity, while CDs promoted A and τ simultaneously. For CDs, it is more important to increase A_{eff}, which highlighted the key role of the effective charge number in photocatalysis. All the above results showed that there was a direct correlation between hydrogen production activity vs. A_{eff}, where 8.75 times increase of A_{eff} from CIZS to CIZS/MoS_2/CDs is almost equal to that of the hydrogen production rate (6.65 times).

3.5. Stability tests and activity optimization of the composite photocatalysts

The effort of MoS_2 and CDs on photocatalytic activity was further investigated by varying their loading amounts. After irradiation for 5 h, the hydrogen yield of pure CIZS was 3.48 mmol g^{-1}. According to Fig. 8a, the hydrogen yield increased with MoS_2 ratio and the optimized CIZS/MoS_2-5% composite reached 8.05 mmol g^{-1}, which was significantly higher than original CIZS. This can be attributed to the fact that the charge separations of both CIZS and MoS_2 were effectively improved with enhanced charge extraction efficiency, leading to the hydrogen production rate of 1.663 mmol g^{-1} h^{-1} for CIZS/MoS_2-5% to, 2.98 times higher than pristine CIZS (0.557 mmol g^{-1} h^{-1}). Then, the hydrogen production rate of the photocatalysts decreased with the increase of MoS_2 loading, which was due to the optical shielding effect caused by excessive MoS_2. Furthermore, the effect CDs was studied in detail by introducing different amount of CDs to CIZS/MoS_2-5% (Fig. 8c). The hydrogen yield of the optimized CIZS/MoS_2/CDs composite reached 18.533 mmol g^{-1}, which was significantly higher than that of the original CIZS/MoS_2-5% binary composite. The addition of CDs could sink the photogenerated electrons and thus increase the number of effective surface charges. As a result, the hydrogen production rate of CIZS/MoS_2/CDs-7% was 3.706 mmol g^{-1} h^{-1} (Fig. 8d) (Table S1), which was 2.32 times of the binary CIZS/MoS_2-5% composite. However, excessive CDs would reduce the production rate of H_2, which might be due to that excessive CDs cover the HER active sites on the surface of MoS_2 and also prevent CIZS/MoS_2/CDs-7% from absorbing light. In a word, the reason for the light shielding effect is the excessive MoS_2 nanosheets and CDs cover the surface of CIZS QDs, which prevents the penetration of incident light, causing the CIZS QDs not fully absorb photons and reducing the amount of photogenerated charge carriers. In addition, excessive MoS_2 nanosheets and CDs lead to the shielding of the active sites on the surface of CIZS QDs [1,41,50]. As discussed above in Fig. 8, the significant improvement of H_2 evolution can be attributed to the suitable band

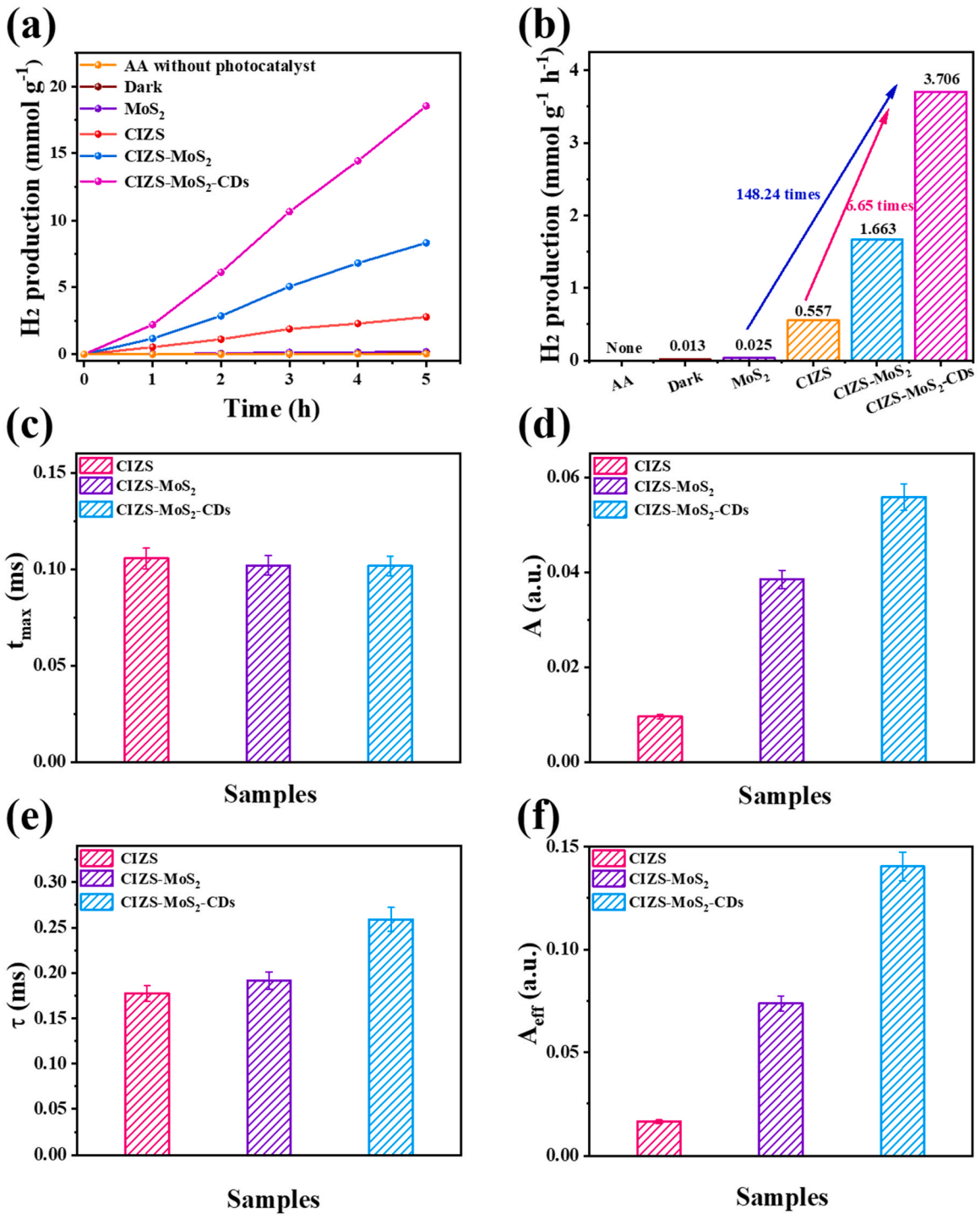

Fig. 7. (a) Amount of the time-dependent hydrogen evolution and (b) hydrogen evolution rate of AA without photocatalyst, dark reaction (with CIZS/MoS_2/CDs), MoS_2 nanosheets, CIZS QDs, CIZS/MoS_2 and CIZS/MoS_2/CDs photocatalysts. Comparison of (c) t_{max}, (d) A, (e) τ and (f) A_{eff} of the samples.

alignment that ensures the efficient charge separation where MoS_2 and CDs acted as electron cocatalysts. More importantly, the addition of CDs sinks the charge carriers and improves the carrier lifetime and subsequently the efficiency of charge separation. To further explore the nanocomposites in comparison with the absorption spectra, we have performed the photocatalytic hydrogen evolution at different wavelengths and calculated the corresponding AQE. As demonstrated in Fig. S7, the wavelength-dependent AQE reached 31.03% at 420 nm, 34.23% at 450 nm, 29.71% at 485 nm, 6.65% at 520 nm, 3.30% at 595 nm and 1.22% at 630 nm, respectively, which were in good agreement with the light absorption of CIZS/MoS_2/CDs. As the wavelength increases, AQE gradually decreases, and can be ignored when the wavelength exceeds 630 nm. The CIZS/MoS_2/CDs composite shows one of the best photocatalytic H_2 production rates and AQEs relative to that reported in the recent works [26,35,38]. The cycle stability of photocatalysts was also very significant. In Fig. 8e, the cycle stability of pure CIZS QDs, CIZS/MoS_2 and CIZS/MoS_2/CDs was also studied through four photocatalytic hydrogen production cycles. For pure CIZS QDs and binary CIZS/MoS_2, the slope of hydrogen production curve indicates a downward trend in the third cycle. Whereas CIZS/MoS_2/CDs did not

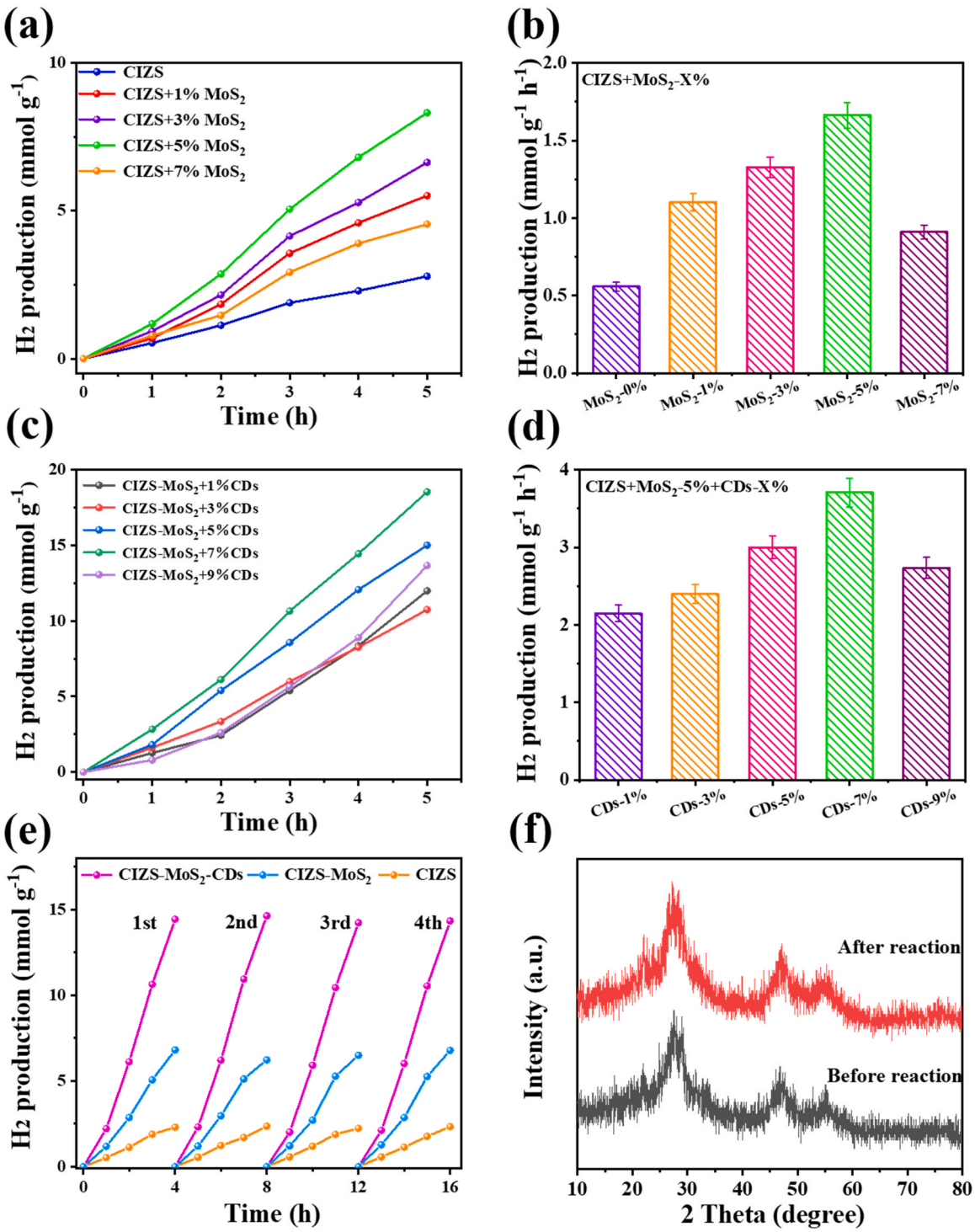

Fig. 8. (a) Amount of hydrogen production and (b) hydrogen production rate of the samples with different amounts of MoS_2 in CIZS/MoS_2 composites. (c) Amount of hydrogen production and (d) hydrogen production rate of the samples with different amounts of CDs in CIZS/MoS_2/CDs composites. (e) Cycle stability of hydrogen production over CIZS, CIZS/MoS_2 and CIZS/MoS_2/CDs. (f) XRD patterns of CIZS/MoS_2/CDs nanocomposites before and after photocatalytic hydrogen production.

show any downward trend in all the four hydrogen production cycles. This shows that the electron sinking effect of CDs effectively promotes the charge transfer kinetics and improves the stability of the CIZS/-MoS_2/CDs composites. The hydrogen production rate was almost unchanged in four cycles within 16 h. To further explore the stability of CIZS/MoS_2/CDs after photocatalytic hydrogen production, XRD, TEM and XPS of used CIZS/MoS_2/CDs were carried out after irradiation. There was almost no change in the XRD patterns after a long time of light reaction (Fig. 8f), indicating the structure robustness of the CIZS/MoS_2/CDs composites. As displayed in Fig. S8, it can be seen from the TEM image that similar flakes are loaded with agglomerated black dots, e.g. CDs and CIZS QDs. As a result, the appearance of the catalyst still presents a close 0D/2D heterojunction structure as before, which proves the structural stability of the photocatalyst. XPS also confirmed that the stability of the material has no obvious change through high-resolution spectra of Cu, In, Mo and S on the used CIZS/MoS_2/CDs after irradiation, as demonstrated in Fig. S9. These results clearly exhibited that the CIZS/MoS_2/CDs nanocomposites had excellent

photocatalytic stability, where the photo-corrosion of CIZS could be inhibited after loading the two cocatalysts due to effective electron-hole separation and sinking. In order to further explain the mechanism, photoelectrochemical tests were performed on these samples.

3.6. Mechanism

To further understand the catalytic mechanism, we carried out a series of photoelectrochemical tests. Compared with pure CIZS QDs and CIZS/MoS_2, CIZS/MoS_2/CDs obtains the highest photocurrent (Fig. 9a), indicating more photogenerated charge carriers and effective charge separation [51,52]. Fig. 9b shows the EIS, in which CIZS/MoS_2/CDs shows the smallest arc radius and also the smallest R_{ct} value (Table S2), revealing the fastest charge transfer [53,54]. The steady-state PL spectra (Fig. 9c) shows that CIZS had a strong PL peak at 600 nm, and the introduction of CDs and MoS_2 could effectively quench the PL of QDs. Comparing with pure CIZS QDs, the PL intensity of CIZS/MoS_2/CDs decreased by 94.8%, showing that the electron extraction ability of

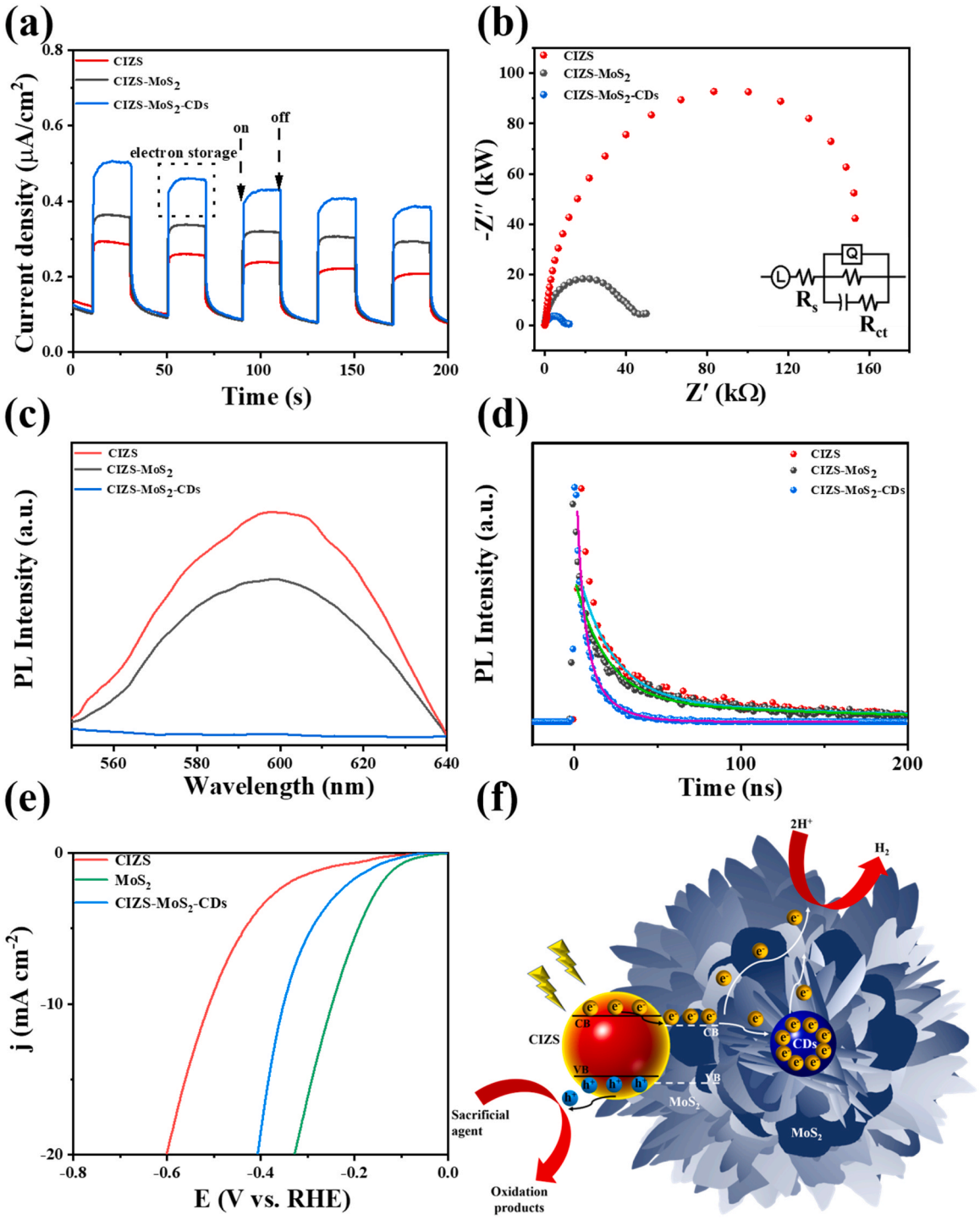

Fig. 9. (a) Transient photocurrent response, (b) EIS spectra (inset in (b): an equivalent circuit of EIS), (c) steady-state PL spectra and (d) time-resolved PL decay curves of CIZS, CIZS/MoS_2 and CIZS/MoS_2/CDs. (e) The LSV curves of CIZS, MoS_2 and CIZS/MoS_2/CDs for HER activity estimation under light irradiation. (f) Schematic mechanism illustration for CIZS/MoS_2/CDs.

MoS_2 and CDs could effectively improve the charge separation. The samples were also characterized by time-resolved PL spectroscopy. As demonstrated in Table S3, the average PL lifetimes of CIZS/MoS_2 (161.17 ns) and CIZS/MoS_2/CDs (12.74 ns) was significantly shorter than that of CIZS QDs (173.24 ns) [55]. It showed that MoS_2 and CDs may extract the electrons in CIZS QDs more effectively and reduce charge recombination. The LSV curves in Fig. 9e was used to analyze the electrocatalytic HER performance of CIZS, MoS_2 and CIZS/MoS_2/CDs, indicating that MoS_2 had the best HER activity under light, which provides the main active sites for hydrogen production. The results declared that the presence of MoS_2 could promote the reduction of H^+ on the surface of CIZS/MoS_2/CDs, while the charge sinking effect of CDs could promote the charge separation.

A plausible mechanism is proposed in Fig. 9f for interfacial charge transfer and electron sinking effect in the composite photocatalyst. When QDs and MoS_2 were excited by light, the photogenerated electrons were transferred to MoS_2 for hydrogen production, which also could be stored in CDs owning to the charge sinking effect. The main contribution of MoS_2 and CDs was as follows: (1) MoS_2 provided the abundant hydrogen evolution active center; (2) The strong electron storage ability of CDs restricted the charge recombination and enhanced the charge separation at the CIZS/MoS_2/CDs interface. The simultaneous introduction of MoS_2 and CDs could enhance the amount of charge extraction, the attenuation constant of the charge recombination process, and more importantly the effective surface charges (A_{eff}). This improvement was attributed to the formation of abundant 0D/2D heterostructures on the two-dimensional MoS_2 nanosheets. The effective charge transfer and tight interface endowed by the 0D/2D bi-cocatalysts significantly improved the efficiency of charge transfer, and finally rendered the CIZS/MoS_2/CDs system high photocatalytic activity.

4. Conclusions

In summary, we have successfully embedded CIZS QDs and CDs on MoS_2 nanosheets to form a three-component photocatalyst by simple hydrothermal treatment, which showed remarkable enhancement on photocatalytic hydrogen production. Notably, TPV spectroscopy and HER test showed that MoS_2 provided the main active sites of HER and CDs increased the attenuation constant of the surface charge carriers (from 0.178 to 0.260 ms) due to its electron sinking effect, which can increase the effective surface electrons used to participate in the surface reaction and prevent electron/hole recombination. After optimization, the optimal hydrogen production rate of CIZS/MoS_2/CDs was increased to 3706 μmol g^{-1} h^{-1}, 6.65 times to that of pure CIZS and 148.24 times to that of MoS_2. This method could be expanded to synthesize excellent photocatalysts by embedding photoactive CDs in MoS_2 and efficient electron sinking to synergistically improve the photocatalytic performance.

CRediT authorship contribution statement

Qitao Chen: Data curation, Investigation, Writing - original draft, Visualization. **Yanhong Liu:** Conceptualization, Funding acquisition, Writing - review & editing. **Xiaoqing Gu:** TPV tests. **Di Li:** Writing - review & editing. **Dongxu Zhang:** Visualization. **Dongqi Zhang:** Preparation of QDs. **Hui Huang:** Funding acquisition, Supervision. **Baodong Mao:** Conceptualization, Funding acquisition, Writing - original draft, Writing - review & editing, Supervision. **Zhenhui Kang:** Funding acquisition, Writing - review & editing, Supervision. **Weidong Shi:** Project administration, Supervision.

Declaration of Competing Interest

The authors declare that they have no known competing financial interests or personal relationships that could have appeared to influence the work reported in this paper.

Acknowledgments

This work was supported by the National Natural Science Foundation of China (21908081, 21501072, 51972216, 51725204, 21771132 and 52041202), the National MCF Energy R&D Program (2018YFE0306105), Innovative Research Group Project of the National Natural Science Foundation of China (51821002), the Jiangsu Specially-Appointed Professors Program, and the Natural Science Foundation of Jiangsu Province (BK20190041, BK20190828 and BK20150489).

Appendix A. Supporting information

Supplementary data associated with this article can be found in the online version at doi:10.1016/j.apcatb.2021.120755.

References

[1] Q. Li, B. Guo, J. Yu, J. Ran, B. Zhang, H. Yan, J.R. Gong, Highly efficient visible-light-driven photocatalytic hydrogen production of CdS-cluster-decorated graphene nanosheets, J. Am. Chem. Soc. 133 (2011) 10878–10884.
[2] Y. Wang, A. Vogel, M. Sachs, R.S. Sprick, L. Wilbraham, S.J.A. Moniz, R. Godin, M. A. Zwijnenburg, J.R. Durrant, A.I. Cooper, J. Tang, Current understanding and challenges of solar-driven hydrogen generation using polymeric photocatalysts, Nat. Energy 4 (2019) 746–760.
[3] Y. Shiraishi, T. Takii, T. Hagi, S. Mori, Y. Kofuji, Y. Kitagawa, S. Tanaka, S. Ichikawa, T. Hirai, Resorcinol-formaldehyde resins as metal-free semiconductor photocatalysts for solar-to-hydrogen peroxide energy conversion, Nat. Mater. 18 (2019) 985–993.
[4] X. Zou, Y. Zhang, Noble metal-free hydrogen evolution catalysts for water splitting, Chem. Soc. Rev. 44 (2015) 5148–5180.
[5] A. Hossain, A. Bhattacharyya, O. Reiser, Copper's rapid ascent in visible-light photoredox catalysis, Science 364 (2019).
[6] P. Wang, S. Guo, H.J. Wang, K.K. Chen, N. Zhang, Z.M. Zhang, T.B. Lu, A broadband and strong visible-light-absorbing photosensitizer boosts hydrogen evolution, Nat. Commun. 10 (2019) 3155.
[7] Z. Zeng, A. Wang, L. Ping, J. Yang, Q. Wang, Encapsulation of lanthanides in ternary I–III–VI $AgInS_2$ nanocrystals and their physical properties, Mater. Lett. 141 (2015) 225–227.
[8] L.M. Zhao, Q.Y. Meng, X.B. Fan, C. Ye, X.B. Li, B. Chen, V. Ramamurthy, C.H. Tung, L.Z. Wu, Photocatalysis with quantum dots and visible light: selective and efficient oxidation of alcohols to carbonyl compounds through a radical relay process in water, Angew. Chem. Int. Ed. 56 (2017) 3020–3024.
[9] P.-Y. Hsieh, T. Kameyama, T. Takiyama, K. Masuoka, T. Yamamoto, Y.-J. Hsu, T. Torimoto, Controlling the visible-light driven photocatalytic activity of alloyed ZnSe–$AgInSe_2$ quantum dots for hydrogen production, J. Mater. Chem. A 8 (2020) 13142–13149.
[10] L. De Trizio, M. Prato, A. Genovese, A. Casu, M. Povia, R. Simonutti, M.J. P. Alcocer, C. D'Andrea, F. Tassone, L. Manna, Strongly fluorescent quaternary Cu–In–Zn–S nanocrystals prepared from $Cu_{1-x}InS_2$ nanocrystals by partial cation exchange, Chem. Mater. 24 (2012) 2400–2406.
[11] W. Jiang, Y. Zhao, X. Zong, H. Nie, L. Niu, L. An, D. Qu, X. Wang, Z. Kang, Z. Sun, Photocatalyst for high-performance H_2 production: Ga-doped polymeric carbon nitride, Angew. Chem. Int. Ed. 60 (2021) 6124–6129.
[12] F. Li, Y. Liu, B. Mao, L. Li, H. Huang, D. Zhang, W. Dong, Z. Kang, W. Shi, Carbon-dots-mediated highly efficient hole transfer in I-III-VI quantum dots for photocatalytic hydrogen production, Appl. Catal. B (2021).
[13] L. Jiang, X. Yuan, Y. Pan, J. Liang, G. Zeng, Z. Wu, H. Wang, Doping of graphitic carbon nitride for photocatalysis: a reveiw, Appl. Catal. B 217 (2017) 388–406.
[14] G. Zhou, Y. Shan, Y. Hu, X. Xu, L. Long, J. Zhang, J. Dai, J. Guo, J. Shen, S. Li, L. Liu, X. Wu, Half-metallic carbon nitride nanosheets with micro grid mode resonance structure for efficient photocatalytic hydrogen evolution, Nat. Commun. 9 (2018) 3366.
[15] S. Luo, J. Ke, M. Yuan, Q. Zhang, P. Xie, L. Deng, S. Wang, $CuInS_2$ quantum dots embedded in Bi_2WO_6 nanoflowers for enhanced visible light photocatalytic removal of contaminants, Appl. Catal. B 221 (2018) 215–222.
[16] S. Song, J. Wang, T. Peng, W. Fu, L. Zan, MoS_2.MoO_{3-x} hybrid cocatalyst for effectively enhanced H_2 production photoactivity of $AgIn_5S_8$ nano-octahedrons, Appl. Catal. B 228 (2018) 39–46.
[17] H. Zhang, P. Zhang, M. Qiu, J. Dong, Y. Zhang, X.W.D. Lou, Ultrasmall MoOx clusters as a novel cocatalyst for photocatalytic hydrogen evolution, Adv. Mater. 31 (2019), 1804883.
[18] S.H. Kim, J. Lim, R. Sahu, O. Kasian, L.T. Stephenson, C. Scheu, B. Gault, Direct imaging of dopant and impurity distributions in 2D MoS_2, Adv. Mater. 32 (2020), 1907235.
[19] J. Hu, L. Yu, J. Deng, Y. Wang, K. Cheng, C. Ma, Q. Zhang, W. Wen, S. Yu, Y. Pan, J. Yang, H. Ma, F. Qi, Y. Wang, Y. Zheng, M. Chen, R. Huang, S. Zhang, Z. Zhao, J. Mao, X. Meng, Q. Ji, G. Hou, X. Han, X. Bao, Y. Wang, D. Deng, Sulfur vacancy-rich MoS_2 as a catalyst for the hydrogenation of CO_2 to methanol, Nat. Catal. 4 (2021) 242–250.

[20] Y. Li, S. Wu, J. Zheng, Y.-K. Peng, D. Prabhakaran, R.A. Taylor, S.C.E. Tsang, 2D photocatalysts with tuneable supports for enhanced photocatalytic water splitting, Mater. Today 41 (2020) 34–43.

[21] X. Liu, Z. Xing, Y. Zhang, Z. Li, X. Wu, S. Tan, X. Yu, Q. Zhu, W. Zhou, Fabrication of 3D flower-like black N-TiO_{2-x}@MoS_2 for unprecedented-high visible-light-driven photocatalytic performance, Appl. Catal. B 201 (2017) 119–127.

[22] T. Taniguchi, L. Nurdiwijayanto, S. Li, H.E. Lim, Y. Miyata, X. Lu, R. Ma, D. M. Tang, S. Ueda, K. Tsukagoshi, T. Sasaki, M. Osada, On/Off boundary of photocatalytic activity between single- and bilayer MoS_2, ACS Nano 14 (2020) 6663–6672.

[23] K. Zhuge, Z. Chen, Y. Yang, J. Wang, Y. Shi, Z. Li, In-suit photodeposition of MoS_2 onto CdS quantum dots for efficient photocatalytic H_2 evolution, Appl. Surf. Sci. 539 (2021), 148234.

[24] X.Y. Liu, H. Chen, R. Wang, Y. Shang, Q. Zhang, W. Li, G. Zhang, J. Su, C.T. Dinh, F. P.G. de Arquer, J. Li, J. Jiang, Q. Mi, R. Si, X. Li, Y. Sun, Y.T. Long, H. Tian, E. H. Sargent, Z. Ning, ^0D–^2D quantum dot: metal dichalcogenide nanocomposite photocatalyst achieves efficient hydrogen generation, Adv. Mater. 29 (2017), 1605646.

[25] Q. Xiang, J. Yu, M. Jaroniec, Synergetic effect of MoS_2 and graphene as cocatalysts for enhanced photocatalytic H_2 production activity of TiO_2 nanoparticles, J. Am. Chem. Soc. 134 (2012) 6575–6578.

[26] H. Zhao, Z. Jiang, K. Xiao, H. Sun, H.S. Chan, T.H. Tsang, S. Yang, P.K. Wong, Photo-assisted separation of noble-metal-free oxidation and reduction cocatalysts for graphitic carbon nitride nanosheets with efficient photocatalytic hydrogen evolution, Appl. Catal. B: Environ. 280 (2021), 119456.

[27] X. Hai, K. Chang, H. Pang, M. Li, P. Li, H. Liu, L. Shi, J. Ye, Engineering the edges of MoS_2 (WS_2) crystals for direct exfoliation into monolayers in polar micromolecular solvents, J. Am. Chem. Soc. 138 (2016) 14962–14969.

[28] P.C. Shen, C. Su, Y. Lin, A.S. Chou, C.C. Cheng, J.H. Park, M.H. Chiu, A.Y. Lu, H. L. Tang, M.M. Tavakoli, G. Pitner, X. Ji, Z. Cai, N. Mao, J. Wang, V. Tung, J. Li, J. Bokor, A. Zettl, C.I. Wu, T. Palacios, L.J. Li, J. Kong, Ultralow contact resistance between semimetal and monolayer semiconductors, Nature 593 (2021) 211–217.

[29] C. Zhu, C. Liu, Y. Zhou, Y. Fu, S. Guo, H. Li, S. Zhao, H. Huang, Y. Liu, Z. Kang, Carbon dots enhance the stability of CdS for visible-light-driven overall water splitting, Appl. Catal. B 216 (2017) 114–121.

[30] S. Zhao, C. Li, L. Wang, N. Liu, S. Qiao, B. Liu, H. Huang, Y. Liu, Z. Kang, Carbon quantum dots modified MoS_2 with visible-light-induced high hydrogen evolution catalytic ability, Carbon 99 (2016) 599–606.

[31] R.-B. Wei, Z.-L. Huang, G.-H. Gu, Z. Wang, L. Zeng, Y. Chen, Z.-Q. Liu, Dual-cocatalysts decorated rimous CdS spheres advancing highly-efficient visible-light photocatalytic hydrogen production, Appl. Catal. B 231 (2018) 101–107.

[32] Q. Wu, J. Cao, X. Wang, Y. Liu, Y. Zhao, H. Wang, Y. Liu, H. Huang, F. Liao, M. Shao, Z. Kang, A metal-free photocatalyst for highly efficient hydrogen peroxide photoproduction in real seawater, Nat. Commun. 12 (2021) 483.

[33] Y. Zhang, Y. Zhao, Z. Xu, H. Su, X. Bian, S. Zhang, X. Dong, L. Zeng, T. Zeng, M. Feng, L. Li, V.K. Sharma, Monitoring graphene oxide's efficiency for removing Re(VII) and Cr(VI) with fluorescent silica hydrogels, Environ. Pollut. 262 (2020), 114246.

[34] Q. Zhao, C. Yang, H.B. Zhao, G.F. Gao, T.S. Jiang, Fabrication of ternary structure photocatalyst CdS/CQD@mpg-C_3N_4 with enhanced photocatytic performance based on synergistic effect, Chemistryselect 3 (2018) 11824–11834.

[35] B. Luo, Y.Z. Wang, D. Li, H. Shen, L.X. Xu, Z. Fang, Z. Xia, J. Ren, W. Shi, Y.C. Yong, A periplasmic photosensitized biohybrid system for solar hydrogen production, Adv. Energy Mater. 11 (2021), 2100256.

[36] Q.A. Akkerman, A. Genovese, C. George, M. Prato, I. Moreels, A. Casu, S. Marras, A. Curcio, A. Scarpellini, T. Pellegrino, L. Manna, V. Lesnyak, From Binary Cu2S to ternary Cu-In-S and quaternary Cu-In-Zn-S nanocrystals with tunable composition via partial cation exchange, ACS Nano 9 (2015) 521–531.

[37] Y. Xu, T. Chen, Z. Xie, W. Jiang, L. Wang, W. Jiang, X. Zhang, Highly efficient Cu-In-Zn-S/ZnS/PVP composites based white light-emitting diodes by surface modulation, Chem. Eng. J. 403 (2021), 126372.

[38] Y. Wang, X. Liu, J. Liu, B. Han, X. Hu, F. Yang, Z. Xu, Y. Li, S. Jia, Z. Li, Y. Zhao, Carbon quantum dot implanted graphite carbon nitride nanotubes: excellent charge separation and enhanced photocatalytic hydrogen evolution, Angew. Chem. Int. Ed. 57 (2018) 5765–5771.

[39] X.H. Li, T.S. Li, Y.J. Ma, Q. Wei, W.B. Qiu, H.R. Guo, X.F. Shi, P. Zhang, A.M. Asiri, L. Chen, B. Tang, X.P. Sun, Boosted electrocatalytic N_2 reduction to NH_3 by defect-rich MoS_2 nanoflower, Adv. Energy Mater. 8 (2018), 1801357.

[40] D. Zhang, B. Mao, D. Li, Y. Liu, F. Li, W. Dong, T. Jiang, W. Shi, 0D/2D Z-scheme heterojunctions of Zn-$AgIn_5S_8$ QDs/α-Fe_2O_3 nanosheets for efficient visible-light-driven hydrogen production, Chem. Eng. J. (2020).

[41] G. Gong, Y. Liu, B. Mao, L. Tan, Y. Yang, W. Shi, Ag doping of Zn-In-S quantum dots for photocatalytic hydrogen evolution: Simultaneous bandgap narrowing and carrier lifetime elongation, Appl. Catal. B 216 (2017) 11–19.

[42] B. Mao, C.-H. Chuang, J. Wang, C. Burda, Synthesis and photophysical properties of ternary I–III–VI $AgInS_2$ nanocrystals: intrinsic versus surface states, J. Phys. Chem. C. 115 (2011) 8945–8954.

[43] J.M. Wu, W.E. Chang, Y.T. Chang, C.K. Chang, Piezo-catalytic effect on the enhancement of the ultra-high degradation activity in the dark by single- and few-layers MoS_2 nanoflowers, Adv. Mater. 28 (2016) 3718–3725.

[44] W. Li, Y. Zhao, Y. Liu, M. Sun, G.I.N. Waterhouse, B. Huang, K. Zhang, T. Zhang, S. Lu, Exploiting Ru-induced lattice strain in CoRu nanoalloys for robust bifunctional hydrogen production, Angew. Chem. Int. Ed. 60 (2021) 3290–3298.

[45] S. Zang, G. Zhang, Z.-A. Lan, D. Zheng, X. Wang, Enhancement of photocatalytic H_2 evolution on pyrene-based polymer promoted by MoS_2 and visible light, Appl. Catal. B 251 (2019) 102–111.

[46] Y. Yang, B. Mao, G. Gong, D. Li, Y. Liu, W. Cao, L. Xing, J. Zeng, W. Shi, S. Yuan, In-situ growth of Zn–$AgIn_5S_8$ quantum dots on g-C_3N_4 towards 0D/2D heterostructured photocatalysts with enhanced hydrogen production, Int. J. Hydrog. Energy 44 (2019) 15882–15891.

[47] M. Gao, K. Le, G. Wang, Z. Wang, F. Wang, W. Liu, J. Liu, Core-shell $Cu_{2-x}S$ @ CoS_2 heterogeneous nanowire array with superior electrochemical performance for supercapacitor application, Electrochim. Acta 323 (2019), 134839.

[48] E.A. Davis, N.F. Mott, Conduction in non-crystalline systems V. Conductivity, optical absorption and photoconductivity in amorphous semiconductors, Philos. Mag. (Abingdon) 22 (1970) 0903–0922.

[49] Y. Liu, Y. Zhao, Q. Wu, X. Wang, H. Nie, Y. Zhou, H. Huang, M. Shao, Y. Liu, Z. Kang, Charge storage of carbon dot enhances photo-production of H_2 and H_2O_2 over Ni_2P/carbon dot catalyst under normal pressure, Chem. Eng. J. 409 (2021), 128184.

[50] A. Meng, L. Zhang, B. Cheng, J. Yu, Dual cocatalysts in TiO_2 photocatalysis, Adv. Mater. 31 (2019), 1807660.

[51] Y. Qin, H. Li, J. Lu, F. Meng, C. Ma, Y. Yan, M. Meng, Nitrogen-doped hydrogenated TiO_2 modified with CdS nanorods with enhanced optical absorption, charge separation and photocatalytic hydrogen evolution, Chem. Eng. J. 384 (2020), 123275.

[52] L. Jing, Y. Xu, M. Xie, J. Liu, J. Deng, L. Huang, H. Xu, H. Li, Three dimensional polyaniline/$MgIn_2S_4$ nanoflower photocatalysts accelerated interfacial charge transfer for the photoreduction of Cr(VI), photodegradation of organic pollution and photocatalytic H_2 production, Chem. Eng. J. 360 (2019) 1601–1612.

[53] D. Zhang, W. Cao, B. Mao, Y. Liu, F. Li, W. Dong, T. Jiang, Y.-C. Yong, W. Shi, Efficient 0D/2D heterostructured photocatalysts with Zn-$AgIn_5S_8$ quantum dots embedded in ultrathin NiS nanosheets for hydrogen production, Ind. Eng. Chem. Res. 59 (2020) 16249–16257.

[54] B. Chen, B. Ge, S. Fu, Q. Li, X. Chen, L. Li, J. Wang, Z. Yang, J. Ding, W. Fan, B. Mao, W. Shi, Ex-situ flame co-doping of tin and tungsten ions in TiO_2 nanorod arrays for synergistic promotion of solar water splitting, Chem. Eng. Sci. 226 (2020), 115843.

[55] M. Liu, L.-Z. Qiao, B.-B. Dong, S. Guo, S. Yao, C. Li, Z.-M. Zhang, T.-B. Lu, Photocatalytic coproduction of H_2 and industrial chemical over MOF-derived direct Z-scheme heterostructure, Appl. Catal. B: Environ. 273 (2020), 119066.